

# Mesoscale models and uniaxial tensile numerical simulations of concrete considering material heterogeneity and spatial correlation

Zhishan Zheng<sup>1</sup>, Xiaosheng Wei<sup>1</sup>, Cong Tian\*

School of Civil and Hydraulic Engineering, Huazhong University of Science and Technology, Wuhan 430074, China



## ARTICLE INFO

### Keywords:

Concrete Mesoscale Concretization Model  
Heterogeneity  
Spatial correlation  
Uniaxial tensile  
Numerical simulation

## ABSTRACT

Concrete is a typical heterogeneous material with initial defects. Its internal structure is very complex and has unique mechanical and physical properties. At the mesoscale, concrete is regarded as a heterogeneous composite material composed of multiphase. A new procedure named “mesh – placement – identification – assignment” (MPIA) was proposed to establish the mesoscale model and assign material properties to each phase. The innovation of this work is that the assigned material properties can and effectively characterize the heterogeneity (randomness), continuity, and correlation of each phase in concrete. Weibull’s statistical distribution function was used to describe the heterogeneity of material properties, and the spatial correlation coefficient was introduced to consider the correlation and continuity of materials in space. Considering the ITZs as a part of mortar, the concrete is regarded as a two-phase composite material composed of aggregate and mortar. The proposed model named Concrete Mesoscale Concretization Model (Double CM) can effectively characterize the transition and transformation of mechanical properties from the surface of aggregate to the mortar interior. The uniaxial tensile simulation results show that the tensile strength of concrete can be improved by increasing the homogeneous degree, increasing the aggregate content, and using crushed stone aggregate. The increase of the spatial correlation coefficient will result in the concentrated distribution of the weak parts in concrete and decrease the tensile strength of concrete.

## 1. Introduction

Concrete is widely used in constructing infrastructures such as buildings and bridges due to its wide range of raw materials and low cost. To solve the practical engineering problems, the inhomogeneity of concrete is usually ignored, and the concrete is considered homogeneous in macroscopic. However, this simplified method cannot describe the failure modes of crack initiation, propagation, and instability of concrete under load. In order to solve the above problems, numerical simulations based on the concrete mesoscale models have been developed rapidly [1–6]. Generally speaking, concrete is regarded as a three-phase heterogeneous composite material composed of aggregate, mortar, and interface transition zone (ITZ) at the mesoscale [7–8]. ITZ is the interface between aggregate and mortar, which is the weakest link in concrete due to the high porosity. Under the action of external load, the internal micro-cracks of concrete often appear in the ITZ and then gradually develop and penetrate the mortar, which eventually leads to

destructive macro cracks in the concrete [9–10].

Before the numerical simulation, it is necessary to establish the mesoscale model that meets the requirements, which is called pre-treatment [11]. At present, the commonly used methods for establishing concrete mesoscale models are mainly divided into the following four categories: (1) The geometric aggregates are generated firstly and then randomly placed [7,12–13]. When the content of the aggregates that have been placed is large, a large number of intersection judgment algorithms are required to place new aggregates since most of the space is occupied by the aggregates that have been placed, so the efficiency of placing is extremely low. (2) The base aggregates are placed first and then grow base aggregates [14]. (3) The method is based on the Voronoi diagram [15–16]. This method combines the process of aggregate generation and placement, which can improve the model generation speed because the intrusion detection of aggregate is not required. However, it is difficult to control the shape and gradation of aggregate. (4) Using computer image analysis and X-ray computer tomography technology

\* Corresponding author.

E-mail address: [1303759761@qq.com](mailto:1303759761@qq.com) (C. Tian).

<sup>1</sup> Address: Room 201, West building No.6, School of Civil and Hydraulic Engineering, Huazhong University of Science and Technology, 1037 Luoyu Road, Wuhan 430074, China.

[17–18]. However, the limitation of this technique is that the process of sample preparation, cutting, and scanning is time-consuming and expensive.

In the study of the mechanical properties of mesoscale concrete, for simplification, the various phase materials, namely aggregate, mortar and ITZ, are usually regarded as uniformly distributed in the space [19]. However, the actual aggregate or matrix contains many random micro-pores and defects, and this simplification ignores the randomness inside the concrete. Some scholars assumed that the properties of each phase material in the concrete satisfy the Weibull distribution, and the material properties are completely randomly distributed in space [20–21]. However, the material properties are actually not completely randomly distributed and disorderly but show a certain correlation in the local scope of space, and this continuity and correlation have not been studied in depth at present. Therefore, careful consideration of each phase of concrete's randomness, continuity, and correlation in the mesoscale model is the focus and innovation of this work.

In the mixing and vibration forming process, concrete will bleed on the surface of aggregate due to different densities of each component, resulting in excessive water-cement ratio and high porosity. Calcium hydroxide with low compactness is directionally generated along with the aggregate, resulting in poor mechanical properties. In general, these areas with poor mechanical properties are called interfacial transition zones (ITZ) [3,6]. In fact, these weak areas are also part of the mortar. Therefore, it is a meaningful work to regard the ITZ as the weak mortar and adopt a suitable method to characterize the transition and transformation of the mechanical properties from the surface of the aggregate to the interior of the mortar.

In addition, as an artificial quasi-brittle material, concrete is susceptible to tensile stress. The traditional macro models assume that concrete is homogeneous, which cannot accurately describe the process of crack initiation, propagation, and penetration in concrete under external loads [22]. At present, there is no research to observe the evolution of cracks based on the careful consideration of the randomness, continuity, and correlation of each phase of concrete. The failure mechanism of mesoscale concrete with heterogeneous materials of various phases under external load remains studied.

In this paper, a complete procedure named “mesh – placement – identification – assignment” (MPIA) is proposed to establish the mesoscale model and assign material properties to each phase. The task of “mesh” is to divide regular finite element meshes in advance, mainly completed by the background grid method, corresponding to Section 2 of this paper. The steps of “placement” and “identification” are used to place aggregates with different shapes and identify the materials of different phases, respectively, corresponding to Section 3 of this paper. The “assignment” step is used to assign material properties to each phase. In Section 4, four different methods for assigning material properties are introduced: Homogeneous, Weibull, Spatially-correlated (three-phase), Spatially-correlated (two-phase). In Section 5, the mesoscale models of concrete obtained by different material properties assignment methods are verified by uniaxial tension simulations. The effects of homogeneous degree and spatial correlation coefficient on the simulation results are analyzed based on the Spatially-correlated (two-phase) method for assigning material properties and the effects of aggregate shape and aggregate content on the tensile strength of concrete are discussed.

## 2. Pre-generation of background grid and aggregate gradation setting

### 2.1. Pre-generated background grid

The finite element mesh elements divided by the background grid method are of high quality and uniform size, which is beneficial to the finite element calculation [14]. First, it is necessary to specify the size of the concrete sample (for 2-D case:  $L \times H$ , 3-D case:  $L \times W \times H$ ) and

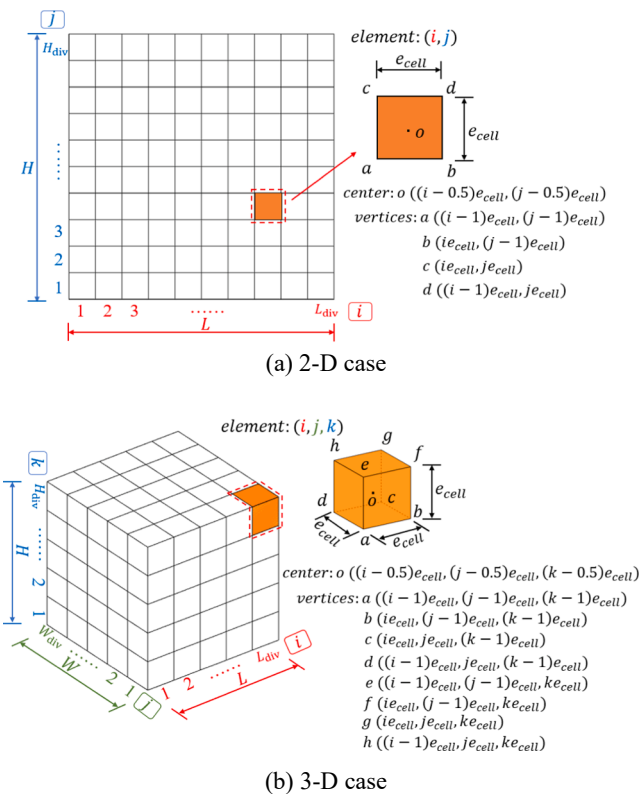


Fig. 1. Background grid calculation schematic diagram.

element size  $e_{cell}$ . It should be noted that the element size needs to be divisible by each side of the concrete sample. The value of the element size should be reasonable. The large element size causes the aggregate outline to be displayed inaccurately, while the small element size leads to the increase of element number and calculation time. The number of elements in each direction of the model is  $L_{div} = L/e_{cell}$ ,  $H_{div} = H/e_{cell}$  (for 3-D cases, it needs to be increased:  $W_{div} = W/e_{cell}$ ). Therefore, the total number of elements in the whole model is  $N_{elem} = L_{div} \times H_{div}$  for the 2-D case and  $N_{elem} = L_{div} \times W_{div} \times H_{div}$  for the 3-D case. For the 2-D case,  $i$  and  $j$  represent the sequence numbers of the element in the length and height directions, respectively, and the coordinate calculation details of the four vertices  $a, b, c, d$ , and the center point  $o$  of the element  $(i, j)$  are shown in Fig. 1(a). For the 3-D case,  $i, j$ , and  $k$  represent the sequence numbers of the element in the length, width, and height directions, respectively. The coordinate calculation details of the eight vertices  $a, b, c, d, e, f, g, h$  and the center point  $o$  of the element  $(i, j, k)$  are shown in Fig. 1(b).

### 2.2. Aggregate gradation

The aggregate gradation includes two aspects: (1) the size of the aggregate particles, (2) the number of aggregates of each particle size, that is, the particle size distribution. For ordinary concrete, coarse aggregate is defined as particles with a particle size greater than 4.75 mm, and coarse aggregate accounts for about 40–50% of the volume of concrete [7]. The ideal gradation is composed of aggregates with different particle sizes by a certain content [23]. If the contents of each aggregate size are close to the ideal continuous gradation curve, the configured concrete will obtain greater compactness and higher strength. The Fuller gradation curve is adopted in this paper, as shown in Eq. (1) [11].

$$P(d) = 100 \left( \frac{d}{d_{max}} \right)^n \quad (1)$$

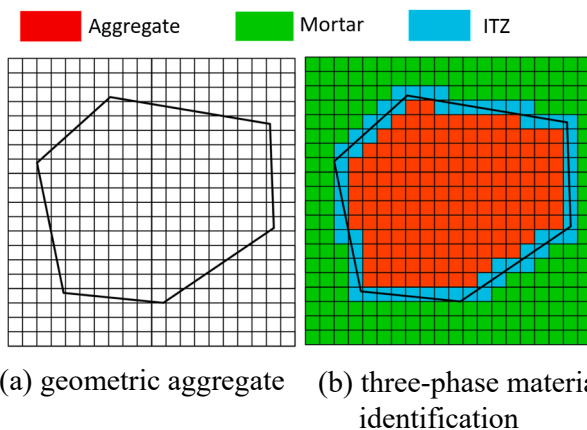


**Fig. 2.** Principle of the background grid method based on element nodes.

where  $P(d)$  is the volume fraction of aggregate passing through the sieve size  $d$ ;  $d_{max}$  represents the maximum particle size of the aggregate;  $n$  is an empirical parameter in the range of 0.45–0.7 (0.5 is adopted in this paper) [15].

Assuming that the volume fraction of aggregate in the concrete sample is  $v_p$ , according to Eq. (1), the volume fraction of aggregate within the particle size range  $[d_i, d_{i+1}]$  is:

$$v_{[d_i, d_{i+1}]} = \frac{P(d_{i+1}) - P(d_i)}{P(d_{max}) - P(d_{min})} \times v_p \quad (2)$$

In order to ensure the equivalence with the 3D gradation, Walraven deduced the transformation formula of the Fuller curve in 2D, as shown in Eq. (3) [24].

$$P(D < D_0) = P_k \left[ 1.065 \left( \frac{D_0}{D_{max}} \right)^{0.5} - 0.053 \left( \frac{D_0}{D_{max}} \right)^4 - 0.012 \left( \frac{D_0}{D_{max}} \right)^6 - 0.0045 \left( \frac{D_0}{D_{max}} \right)^8 + 0.0025 \left( \frac{D_0}{D_{max}} \right)^{10} \right] \quad (3)$$

where  $P(D < D_0)$  represents the area fraction of the aggregate particle size  $D$  less than  $D_0$ ;  $P_k$  is the total area fraction of the aggregate in the concrete sample;  $D_{max}$  is the maximum particle size of the aggregate.

It should be noted that the mesoscale model established in this paper can not only use the gradation curve calculated by the above formula but also can be defined according to the actual aggregate gradation in the experiment.

### 3. Material identification and aggregate placement

#### 3.1. Material identification and aggregate placement rules

##### 3.1.1. Identification principle of the background grid method

From the mesoscale level, ordinary concrete is usually regarded as a three-phase composite material composed of aggregate, mortar, and ITZ [25]. For the traditional mesoscale model establishment methods, such as the “take and place” method, the geometric aggregate is usually placed first, and then the mesh is divided.

On the one hand, the placement of geometric aggregates requires complex intrusion algorithms; on the other hand, meshing and material identification of each phase is also very complicated. In order to reduce the complexity of the algorithms and improve the computational efficiency, the background grid generated in Section 2 is used to assist in the placement of aggregates and the identification of each phase material. For simplification, this section explains the identification principle in the 2D case, which is similar to the 3D case.

The principle of the traditional background grid method based on element nodes to identify element materials is shown in Fig. 2: (1) when all nodes of the element are outside the geometric aggregate, the element is identified as mortar; (2) when all the nodes of the element are inside the geometric aggregate, the element is identified as aggregate; (3) in other cases, the element is identified as ITZ. However, the mesh obtained by this method cannot show the contour of the aggregate well, and the aggregate element content is less than the actual aggregate content.

In this paper, the background grid method based on the element centroid proposed in [14] is adopted to identify materials, as shown in Fig. 3.

The principle of this method is that the element is identified as aggregate when the centroid of the element is inside the geometric

aggregate. The specific material identification steps are as follows:

- (1) The background grid is initialized as mortar at first. That is, all elements are identified as mortar, as shown in Fig. 3(a).
- (2) Identify the aggregate elements by judging whether the centroids of the elements in the red rectangular box in Fig. 3(b) are inside the geometric aggregate. The range of the red rectangular box is determined according to the maximum and minimum coordinates of the geometric aggregate.

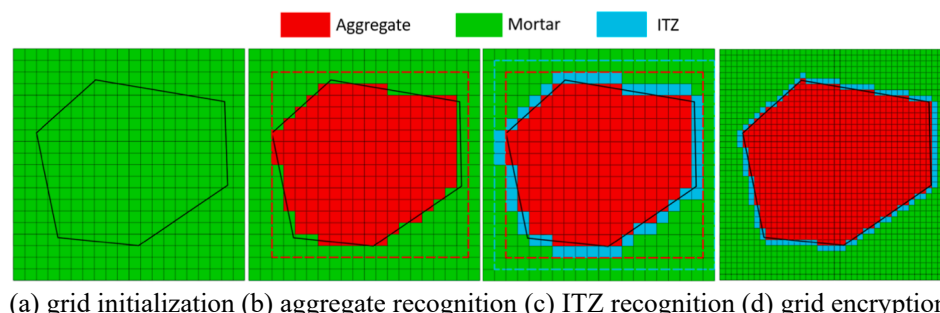


**Fig. 3.** Principle of the background grid method based on element centroid.

- (3) Identify the ITZ elements by judging whether the mortar elements in the blue rectangular box in Fig. 3(b) are adjacent to the geometric aggregate. The range of the blue rectangular box is obtained by expanding the red rectangular box outward by one element.

Compared with Fig. 2(b) and Fig. 3(c), the background grid method based on element centroid can better show the contour of aggregate. Refining the grid can improve the accuracy of the finite element mesh, as shown in Fig. 3(d), but the subsequent consequence is an increase in computational effort. The actual thickness of ITZ in the concrete is generally considered to be between 10 and 50  $\mu\text{m}$ . Still, the thickness of ITZ in the mesoscale model obtained by the background grid method based on the cell centroid is equal to the element size  $e_{\text{cell}}$ . It is unreasonable to adopt the actual thickness of ITZ considering the limitation of computational effort. Generally, the thickness of ITZ is between 1/4 and 1/8 of the minimum aggregate size [23].

### 3.1.2. Aggregate placement rules

The focus of the establishment of the mesoscale model is the placement of aggregates, which needs to meet four requirements: (1) the randomness of aggregate placement; (2) the aggregate particle size meets the predetermined aggregate gradation; (3) the aggregate content is the same as the actual concrete sample; (4) the aggregates are completely separated. For the above four requirements, the most difficult and time-consuming work is to ensure that the aggregates are completely separated, which often requires complex intersection judgment algorithms and calculation time.

The traditional mesoscale model needs to generate the geometric model first. This process is necessary to detect whether the new aggregate overlaps or intersects with all the existing aggregates. With the increase of aggregate quantity, the computational effort becomes larger, which reduces the calculation efficiency. The method used in this paper generates the regular background grid in advance (see Section 2.1). It then completes the placement of aggregate and material identification simultaneously (see section 3.1.1). The intrusion detection of the aggregate is only carried out in the local scope, which can avoid complicated intrusion detection algorithms. The specific details of aggregate generation and placement are as follows.

- (1) Generate specific geometric aggregate according to the aggregate particle size.
- (2) Randomly select the centroid position of the aggregate, and calculate the range of the aggregate vertex coordinates to obtain the red and blue rectangular boxes in Fig. 3(c). It should be noted that for the complete concrete sample, the aggregate must be within the range of the concrete; for the sample cut from the complete concrete, only the aggregate centroid is required to be within the range of the concrete sample.
- (3) Identify and temporarily store the aggregate element within the scope of the red rectangular box. If the newly identified aggregate element has already been designated as an aggregate element, the new aggregate is considered to invade the existing aggregate and go to Step (2); otherwise, the position of the new aggregate is deemed to be appropriate, so it can be placed and go to step (4).
- (4) Identify the ITZ elements around the aggregate within the scope of the blue rectangular box.

The complete placement and material identification process of an aggregate can be completed using the above steps. It is good to start with the largest particles as it would be more difficult to place them if processed at a later stage [26]. The aggregates used to prepare concrete are usually pebbles and crushed stones. In the 2-D case, circular and oval aggregates are usually used to represent pebbles, and polygonal

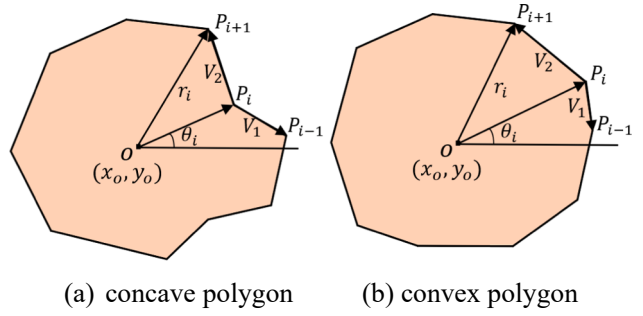


Fig. 4. Polygonal aggregates generated using polar coordinates.

aggregates are used to represent crushed stones. In the 3-D case, sphere and ellipsoid aggregates are usually used to represent pebbles, and polyhedral aggregates are used to represent crushed stones. There are only two differences to place aggregates with different shapes: (1) the control of the aggregate shape; (2) the method to detect whether the point is inside the geometry. In the following section, the placement process for aggregates with different shapes will be introduced respectively.

## 3.2. Generation and placement of 2-D aggregate

### 3.2.1. Circular aggregate

The parameters that control the position and shape of the circular aggregate are the center coordinate  $O(x_o, y_o)$  and the radius  $r$ , respectively. The radius  $r$  of the circular aggregate with particle size in the range of  $[d_i, d_{i+1}]$  can be calculated by Eq. (4).

$$r = d_i/2 + \eta \times (d_{i+1} - d_i)/2 \quad (4)$$

where  $\eta$  is a random variable in the interval  $[0, 1]$ .

The distance between the point  $p_i(x_{p_i}, y_{p_i})$  and the center  $O(x_o, y_o)$  is calculated as  $d_{pi} = \sqrt{(x_o - x_{p_i})^2 + (y_o - y_{p_i})^2}$  to determine whether the point is within the circular aggregate. If  $d_{pi} > r$ , the point is outside the circular aggregate; if  $d_{pi} < r$ , the point is inside the circular aggregate.

### 3.2.2. Oval aggregate

The parameters controlling the position and shape of the oval aggregate are centroid coordinates  $O(x_o, y_o)$ , semi-major axis  $a$ , semi-minor axis  $b$ , and rotation angle  $\theta$ . It is considered that the aggregate can pass through the sieve aperture if the minor axis of the oval aggregate is smaller than the sieve aperture [9]. The semi-minor axis  $b$  and semi-major axis  $a$  of the oval aggregate with the particle size range of  $[d_i, d_{i+1}]$  are calculated by Eq. (5), and the rotation angle  $\theta$  ranges between  $[0, \pi]$ .

$$\begin{cases} b = d_i/2 + \xi \times (d_{i+1} - d_i)/2 \\ a = b/[l + \eta \times (m - l)] \end{cases} \quad (5)$$

where  $\xi$  and  $\eta$  are random variables in the interval  $[0, 1]$ ;  $l$  and  $m$  are the minimum and maximum values of the minor axis ratio to the major axis of the oval aggregate, respectively ( $l = 0.5$  and  $m = 0.8$  are adopted in this paper).

The positional relationship between the point and the ellipse can be determined by the two focal points of the ellipse. The distances  $d_1$  and  $d_2$  between point  $p$  and two focal points  $c_1$  and  $c_2$  of the ellipse are calculated. If  $d_1 + d_2 > 2a$ , point  $p$  is outside the ellipse, if  $d_1 + d_2 = 2a$ , point  $p$  is on the outline of the ellipse, if  $d_1 + d_2 < 2a$ , point  $p$  is inside the ellipse.

### 3.2.3. Polygonal aggregate

The parameters controlling the position and shape of the polygonal aggregate are centroid coordinates  $O(x_o, y_o)$  and vertex coordinates  $P_i$ . To obtain the vertex coordinates within the particle size range  $[d_i, d_{i+1}]$ , a series of polar angles  $\theta_i$  and polar radii  $r_i$  are randomly generated in the polar coordinate system, as shown in Eq. (6).

$$\left\{ \begin{array}{l} \theta_j = 2\pi \times \xi \\ r_j = d_i/2 + \eta \times (d_{i+1} - d_i)/2 \end{array} \right. \quad (6)$$

where the value of subscript  $j$  ranges from 1 to  $n$  ( $n$  is the number of polygon vertices, which is 6–10 in this paper);  $\xi$  and  $\eta$  are random variables in the interval [0,1].

The polygonal aggregates generated by the above method include concave polygons as shown in Fig. 4(a) and convex polygons as shown in Fig. 4(b). The cross-sections of the crushed stones obtained by mechanical crushing are usually convex polygons, so it is necessary to detect the concavity and convexity of the polygon. In this paper, the vector cross product method is used to detect the concavity and convexity of the angles corresponding to the vertices [23]. (1) If  $V_1 \times V_2 > 0$ , the angle corresponding to point  $P_i$  is concave. (2) If  $V_1 \times V_2 < 0$ , the angle corresponding to point  $P_i$  is convex. (3) If  $V_1 \times V_2 = 0$ , the angle corresponding to point  $P_i$  is straight. Polygons with at least one concave angle are concave polygons, which need to be regenerated before placing.

The algorithm for determining the position relationship between points and convex polygons is closely related to the calculation time. The most commonly used and most straightforward method is the area method, but a large amount of calculation leads to low calculation efficiency. This section introduces several other efficient calculation methods: the barycentric coordinate method, the winding number method, and the status matrix method.

#### (1) Barycentric coordinate method

The barycentric coordinates are defined by the vertices of a simplex (such as a triangle or a tetrahedron). Assuming that  $v_1, \dots, v_n$  are the vertices of a simplex in the vector space  $V$ . The coefficients  $(\lambda_1, \dots, \lambda_n)$  are the barycentric coordinates of the point  $P$  concerning  $v_1, \dots, v_n$  if the point  $p$  in  $V$  satisfies Eq. (7).

$$(\lambda_1 + \dots + \lambda_n)p = \lambda_1 v_1 + \dots + \lambda_n v_n \quad (7)$$

For any constant  $k$  that is not equal to zero,  $(k\lambda_1, \dots, k\lambda_n)$  are also the barycentric coordinates of  $p$ . The regularized coordinates satisfy  $\lambda_1 + \dots + \lambda_n = 1$ . A polygon with  $n$  edges can be divided into  $n-2$  triangles, and the barycentric coordinates of point  $p$  for each triangle are calculated respectively. If the point  $p$  is inside the triangle, the corresponding barycentric coordinates are all greater than 0. The barycentric coordinates of the point  $p$  concerning the triangle with vertices  $i, j, k$  can be calculated by Eq. (8).

$$[\lambda_1 \lambda_2 \lambda_3] \begin{bmatrix} 1 & x_i & y_i \\ 1 & x_j & y_j \\ 1 & x_k & y_k \end{bmatrix} = [1 x_p y_p] \quad (8)$$

#### (2) Winding number method

The principle of this method is to calculate the winding number of the polygon that surrounds the point  $R$ . Only when the winding number is zero, the polygon does not surround the point, and the point is outside the polygon [27]. Without loss of generality, assume that the point  $R = (0, 0)$ , each vertex  $P_i$  of the polygon is classified by the quadrant where the vertex is located using Eq. (9).

**Table 1**

Adjusted quadrant angle  $\delta_i^*$ .

$\delta_i$	0	1, -3	-1, 3	2ccw, -2ccw	2cw, -2cw
$\delta_i^*$	0	1	-1	2	-2

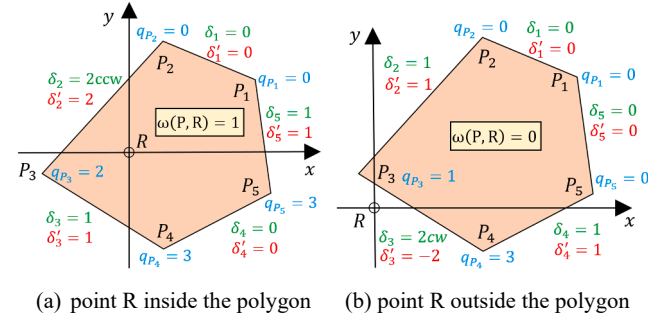


Fig. 5. Winding number method to determine the position relationship between the point and the polygon.

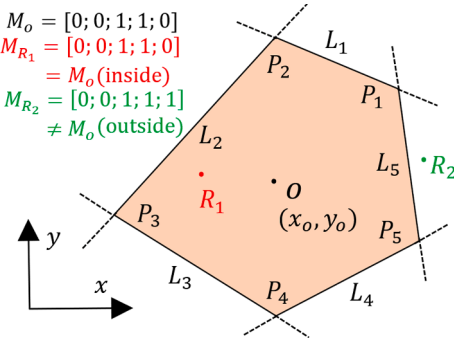


Fig. 6. Status matrix method to determine the position relationship between the point and the polygon.

$$q_{P_i} = \begin{cases} 0 \\ 1 \\ 2 \\ 3 \end{cases} \text{ if } \arctan \frac{y_{P_i}}{x_{P_i}} \in \begin{cases} \left[0, \frac{\pi}{2}\right) \\ \left[\frac{\pi}{2}, \pi\right) \\ \left[\pi, \frac{3\pi}{2}\right) \\ \left[\frac{3\pi}{2}, 2\pi\right) \end{cases} \quad (9)$$

The quadrant angle of each edge of the polygon is defined as  $\delta_i = q_{P_{i+1}} - q_{P_i}$ . There are several situations:  $\delta_i = 0$  indicates that the edge is wholly located in the same quadrant;  $\delta_i \in \{1, -3\}$  indicates that the edge crosses the boundary of a quadrant counterclockwise;  $\delta_i \in \{-1, 3\}$  indicates that the edge crosses the boundary of a quadrant clockwise; When  $\delta_i \in \{-2, 2\}$ , there are two cases of counterclockwise (CCW) and clockwise (CW) respectively, which are calculated by Eq. (10).

$$\operatorname{sign} \begin{vmatrix} x_{P_i} & x_{P_{i+1}} \\ y_{P_i} & y_{P_{i+1}} \end{vmatrix} = \begin{cases} + \\ - \end{cases} \Leftrightarrow \begin{cases} ccw \\ cw \end{cases} \quad (10)$$

The adjusted quadrant angle  $\delta_i^*$  is calculated from Table 1. The winding number of the polygon surrounds the point  $R$  can be calculated from all the adjusted quadrant angles  $\delta_i^*$ , as shown in Eq. (11).

$$\omega(P, R) = \frac{1}{4} \sum_{i=1}^n \delta_i^* \quad (11)$$

The point  $R$  is inside the polygon if  $\omega(P, R) = 1$ , as shown in Fig. 5(a);

**Table 2**

Calculation time (s) of the polygonal aggregate concrete generated by different algorithms.

Method	Calculation time
Area method	0.5303 (6.2364)
Barycentric coordinate method	0.3005
Winding number method	0.2535
Status matrix method	0.1320

and the point is outside the polygon if  $\omega(P, R) = 0$ , as shown in Fig. 5(b). Moreover, the winding number method does not limit the concavity and convexity of the polygon. A more detailed description can be found in the literature [27].

### (3) Status matrix method

The status matrix method is used to determine whether the point is inside the polygon according to the characteristic that the centroid O of a polygon is inside the polygon [28]. First, the linear equation corresponding to each edge  $L_i$  of the polygon is calculated by Eq. (12).

$$f_{L_i}(x, y) = a_i x + b_i y + c_i \quad (12)$$

where  $a_i, b_i, c_i$  are the coefficients of the linear equation corresponding

to the edge  $L_i$ ,  $i = 1, 2, \dots, n$ , and  $n$  is the number of polygon edges.

The positional relationship between the polygon centroid coordinates  $O(x_o, y_o)$  and each edge is recorded in the state matrix  $M_o$  by substituting  $O(x_o, y_o)$  into the linear equation of each side respectively. If  $f_{L_i}(x_o, y_o) \geq 0$ , it indicates that the centroid is on or above the edge, recorded as 1 in  $M_o$ ; if  $f_{L_i}(x_o, y_o) < 0$ , the centroid is below the edge, recorded as 0 in  $M_o$ . The status matrix  $M_{R_i}$  of any point  $R_i$  can be calculated using this method. Comparing the status matrices  $M_{R_i}$  and  $M_o$ , if the two matrices are identical, it can be determined that the point  $R_i$  is inside the polygon, see  $R_1$  in Fig. 6; otherwise, the point  $R_i$  is outside the polygon, see  $R_2$  in Fig. 6.

To compare the efficiency of placing polygonal aggregate by different algorithms, one hundred concrete samples are generated by each method. The average running time is calculated on a laptop configured with Core (TM) i5-7300HQ CPU @ 2.50GHz and 8 GB memory. The factors affecting the generation time of the model include sample size, mesh size, aggregate content, aggregate gradation, etc. Here the concrete sample size is 300 mm × 300 mm, and the grid size is 1 mm (the total amount of grids is 90,000), the aggregate content is 60%, and four-graded (aggregate size: 5–10 mm, 10–20 mm, 20–40 mm, 40–80 mm), the calculation time is shown in Table 2. The value in the bracket in Table 2 refers to the calculation time of the traditional method [23] that first generates the geometric model and then divides the mesh. It can be seen that the method in this paper can speed up by about 90%.

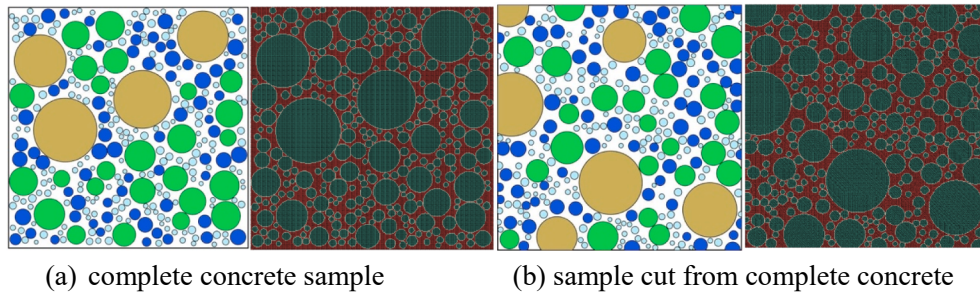


Fig. 7. Geometric models and finite element models of circular aggregate concrete.

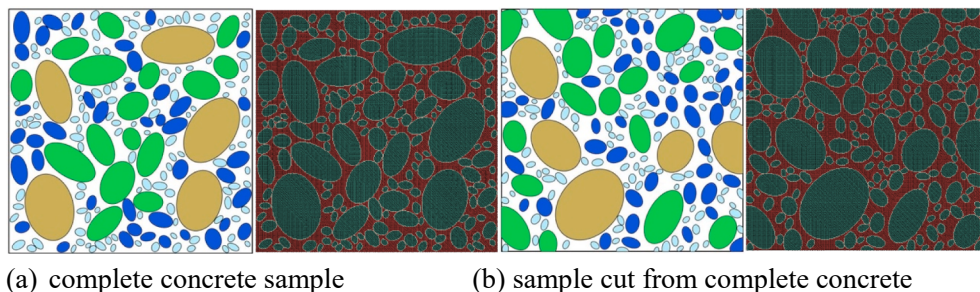


Fig. 8. Geometric models and finite element models of oval aggregate concrete.

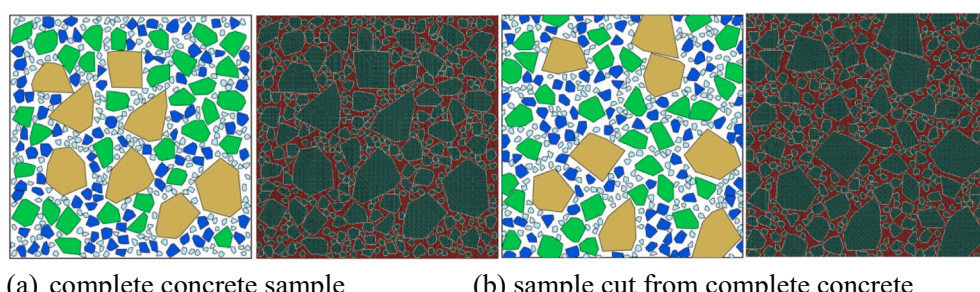


Fig. 9. Geometric models and finite element models of polygonal aggregate concrete.

Among the four methods, the status matrix method is the most efficient, followed by the winding number method, and the third is the barycentric coordinate method. In contrast, the area method has an enormous amount of calculation and the lowest efficiency. Under the same conditions, the time consumed by the status matrix method is only a quarter of the area method.

### 3.2.4. Examples of 2-D mesoscale model

Concrete mesoscale models with different aggregate shapes are generated in the 2-D case, as shown in Figs. 7–9. The concrete sample size is 300 mm × 300 mm, and the grid size is 1 mm, the aggregate content is 60%, and four-graded (aggregate size: 5–10 mm, 10–20 mm, 20–40 mm, 40–80 mm).

### 3.3. Generation and placement of 3-D aggregate

#### 3.3.1. Spherical aggregate

Similar to the circular aggregate, the parameters that control the position and shape of spherical aggregates are spherical center coordinates  $O(x_0, y_0, z_0)$  and radius  $r$ , respectively. The radius  $r$  of the spherical aggregate with particle size in the range of  $[d_i, d_{i+1}]$  is calculated by Eq. (4). The distance between the point  $p_i(x_{p_i}, y_{p_i})$  and the center

$O(x_0, y_0)$  is calculated as  $d_{pi} = \sqrt{(x_0 - x_{p_i})^2 + (y_0 - y_{p_i})^2 + (z_0 - z_{p_i})^2}$  to determine whether the point is within the spherical aggregate. If  $d_{pi} > r$ , the point is outside the spherical aggregate; if  $d_{pi} < r$ , the point is inside the spherical aggregate.

#### 3.3.2. Ellipsoidal aggregate

The parameters controlling the position and shape of the ellipsoidal aggregate are centroid coordinates  $O(x_0, y_0, z_0)$ , semi-major axis  $a$ , semi-mean axis  $b$ , semi-minor axis  $c$ , and rotation angles  $\alpha$ ,  $\beta$ , and  $\gamma$  around the  $x$ ,  $y$ , and  $z$  axes, respectively. It is considered that the aggregate can pass through the sieve aperture if the mean axis of the ellipsoidal aggregate is smaller than the sieve aperture [9]. The three axes of the ellipsoid with particle size in the range of  $[d_i, d_{i+1}]$  are calculated by Eq. (13).

$$\begin{cases} b = d_i/2 + \phi \times (d_{i+1} - d_i)/2 \\ a = b/[l_1 + \eta \times (m_1 - l_1)] \\ c = a \times [l_2 + \xi \times (m_2 - l_2)] \end{cases} \quad (13)$$

where  $\phi$ ,  $\eta$  and  $\xi$  are random variables in the interval  $[0, 1]$ ;  $l_1$  and  $m_1$  are the minimum and maximum values of the ratio of the mean axis to the major axis of the ellipsoid, and  $l_2$  and  $m_2$  are the minimum and maximum values of the ratio of the minor axis to the major axis of the ellipsoid, respectively ( $l_1 = l_2 = 0.5$  and  $m_1 = m_2 = 0.8$  are adopted in this paper).

The rotation angles  $\alpha$ ,  $\beta$ , and  $\gamma$  of the ellipsoid around the  $x$ ,  $y$ , and  $z$  axes are in the range of  $[0, 360^\circ]$ . Using a right-handed coordinate system and using a positive angle to represent any right-handed rotation, perform intrinsic rotations first around the  $z$ -axis through an angle  $\gamma$ , then around the  $y$ -axis through an angle  $\beta$ , and finally around the  $x$ -axis through an angle  $\alpha$ . After performing the rotation, the ellipsoid center is translated from  $(0, 0, 0)$  to  $(x_0, y_0, z_0)$ . If  $(x', y', z')$  are the coordinates of a point on the ellipsoid prior to rotation, and  $(x, y, z)$  are the coordinates of that point after rotation and translation, then

$$\begin{pmatrix} x \\ y \\ z \end{pmatrix} = R_z(\gamma)R_y(\beta)R_x(\alpha) \begin{pmatrix} x' \\ y' \\ z' \end{pmatrix} + \begin{pmatrix} x_0 \\ y_0 \\ z_0 \end{pmatrix} \quad (14)$$

Where,

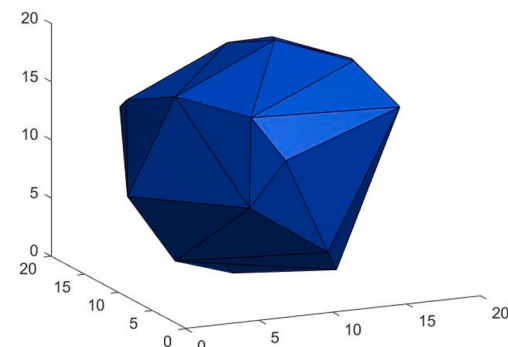


Fig. 10. 3-D random polyhedral aggregate.

$$R_x(\alpha) = \begin{pmatrix} 1 & 0 & 0 \\ 0 & \cos\alpha & -\sin\alpha \\ 0 & \sin\alpha & \cos\alpha \end{pmatrix}, R_y(\beta) = \begin{pmatrix} \cos\beta & 0 & \sin\beta \\ 0 & 1 & 0 \\ -\sin\beta & 0 & \cos\beta \end{pmatrix}, \text{ and } R_z(\gamma) = \begin{pmatrix} \cos\gamma & -\sin\gamma & 0 \\ \sin\gamma & \cos\gamma & 0 \\ 0 & 0 & 1 \end{pmatrix}$$

The ellipsoid equation after rotation and translation is shown in Eq. (15), in which nine parameters can be calculated from the points of the ellipsoid after rotation.

$$F(x, y, z) = Ax^2 + By^2 + Cz^2 + Dxy + Exz + Fyz + Gx + Hy + Iz + 1 \quad (15)$$

The positional relationship between point  $p$  and the ellipsoid is determined by Eq. (15). If  $F(x_p, y_p, z_p) > 0$ , the point is outside the ellipsoid; if  $F(x_p, y_p, z_p) = 0$ , the point is on the outline of the ellipsoid; if  $F(x_p, y_p, z_p) < 0$ , the point is inside the ellipsoid.

#### 3.3.3. Polyhedral aggregate

The vertices of the polyhedron are obtained by randomly selecting points from the auxiliary sphere in the spherical coordinate system. In this paper, the number of vertices  $n$  of the polyhedron is controlled between 15 and 25, which is the same as that in [7, 14, 23]. For the aggregate with particle size within  $[d_i, d_{i+1}]$ , the auxiliary sphere radius  $r$  is calculated by Eq. (4). The polyhedron vertex coordinates  $(x_i, y_i, z_i)$  are calculated by Eq. (16) and Eq. (17).

$$\begin{cases} \theta_i = \eta \times 2\pi \\ \varphi_i = \xi \times 2\pi \end{cases} \quad (16)$$

$$\begin{cases} x_i = r \times \sin\varphi_i \times \cos\theta_i \\ y_i = r \times \sin\varphi_i \times \sin\theta_i \\ z_i = r \times \cos\theta_i \end{cases} \quad (17)$$

where  $\eta$  and  $\xi$  are random variables in the interval  $[0, 1]$ ;  $\theta_i$  and  $\varphi_i$  are the azimuth and zenith angles in the spherical coordinate system, respectively. The vertices of the polyhedron are rotated and translated as a whole by Eq. (14). The shape of the polyhedral aggregate needs to be determined by the geometric topological relationship of the vertices. In this paper, Delaunay triangulation technology and the convex hull algorithm are used to determine the geometric shape of the aggregate, as shown in Fig. 10.

The most commonly used method to judge the position relationship between a point and a polyhedron is the volume method. Still, a large amount of calculation leads to low calculation efficiency. This section introduces two other efficient methods, namely the barycentric coordinate method and the status matrix method.

#### (1) Barycentric coordinate method

**Table 3**

Calculation time (s) of the polyhedral aggregate concrete generated by different algorithms.

Method	Calculation time
Volume method	13,575
Barycentric coordinate method	1002
Status matrix method	208

Similarly, the barycentric coordinate method in Section 3.2.3 is also applicable to the 3-D case. A polyhedron can be decomposed into a series of tetrahedrons. The barycentric coordinates of the point p for each tetrahedron are calculated separately. If the point is inside the tetrahedron, the corresponding barycentric coordinates are all greater than 0. The barycentric coordinates  $(\lambda_1, \lambda_2, \lambda_3, \lambda_4)$  of the point p concerning the tetrahedron with vertices i, j, k, m are calculated by Eq. (18).

$$[\lambda_1 \lambda_2 \lambda_3 \lambda_4] \begin{bmatrix} 1 & x_i & y_i & z_i \\ 1 & x_j & y_j & z_j \\ 1 & x_k & y_k & z_k \\ 1 & x_m & y_m & z_m \end{bmatrix} = [1 x_p y_p z_p] \quad (18)$$

#### (2) Status matrix method

Similarly, the status matrix method in section 3.2.3 is also applicable to the 3-D case, as long as the linear equation in Eq. (12) is extended to the plane equation in Eq. (19).

$$f_i(x, y, z) = a_i x + b_i y + c_i z + d_i \quad (19)$$

To compare the efficiency of placing polyhedral aggregate by different algorithms, thirty concrete samples are generated by each method, and the average running time is calculated. The concrete sample size is set as 100 mm × 100 mm × 100 mm, the grid size is 0.5 mm (the total amount of grids is 8 million), the aggregate content is 30%, and the four-graded (aggregate size: 5–10 mm, 10–15 mm, 15–20 mm, 20–25 mm). The calculation time is shown in Table 3. The status matrix method is the most efficient, followed by the barycentric coordinate method, while the volume method has an enormous amount of calculation and the lowest efficiency. Under the same conditions, the time consumed by the status matrix method is only 1/65 of the volume method.

#### 3.3.4. Examples of 3-D mesoscale model

Concrete mesoscale models with different aggregate shapes are generated in the 3-D case, as shown in Figs. 11–13. The concrete sample size is 100 mm × 100 mm × 100 mm, the grid size is 0.5 mm, the aggregate content is 60%, and the aggregate particle size range is 5–25 mm.

#### 4. Material properties assignment

Concrete is a discontinuous and inhomogeneous composite material that can be regarded as composed of aggregate, mortar, and ITZ at the mesoscale level. For simplification, scholars usually treated each phase

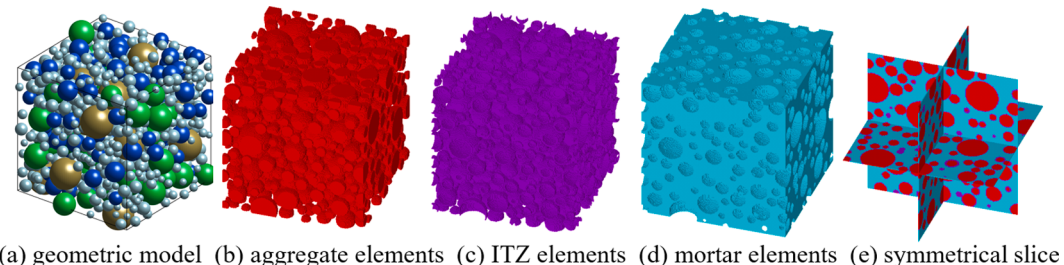


Fig. 11. Geometric model and finite element model of spherical aggregate concrete.

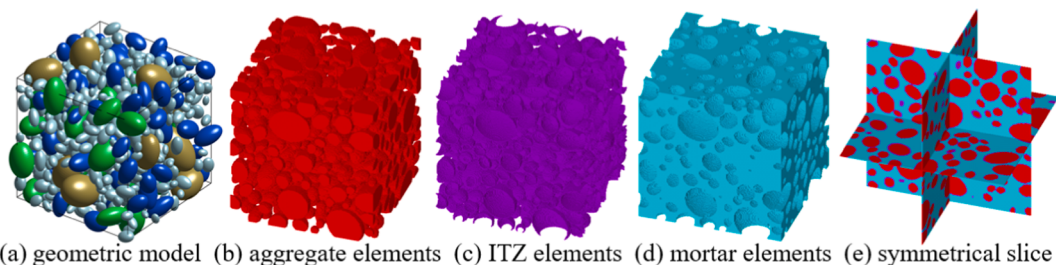


Fig. 12. Geometric model and finite element model of ellipsoidal aggregate concrete.

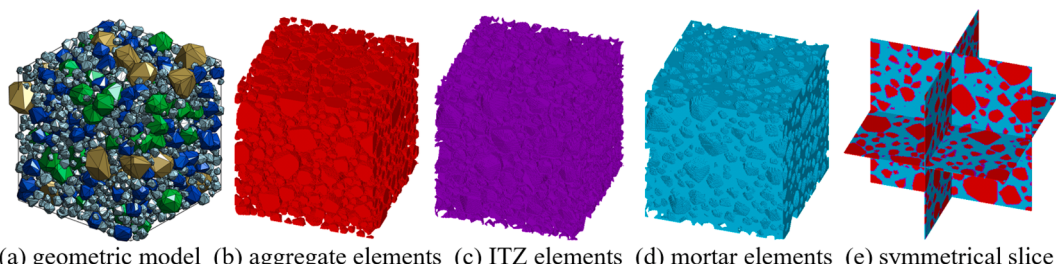
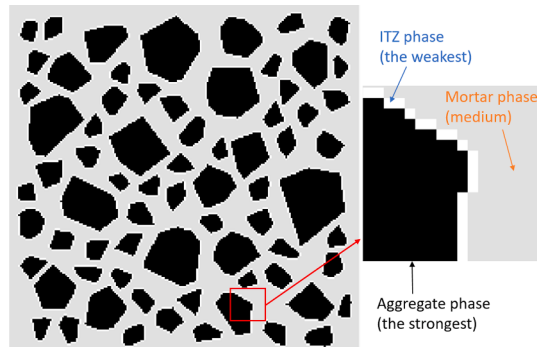
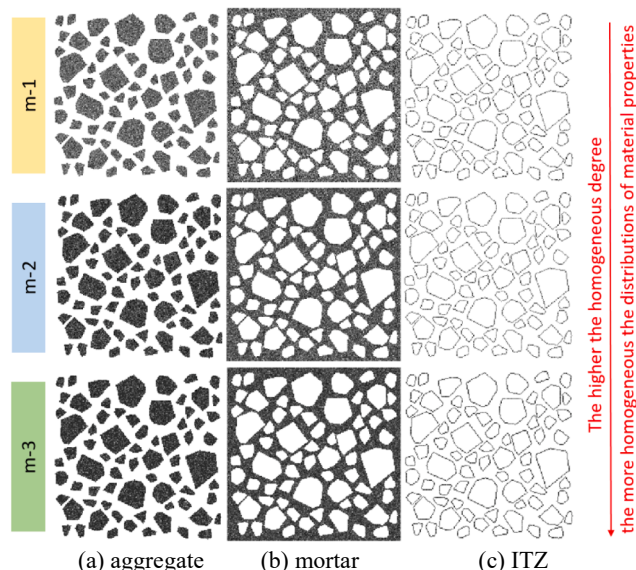


Fig. 13. Geometric model and finite element model of polyhedral aggregate concrete.

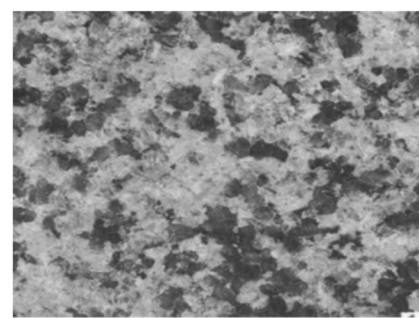
**Table 4**

Elastic modulus and homogeneous degree of each phase material.

Material	Elastic modulus/GPa	Homogeneous degree		
		m-1	m-2	m-3
Aggregate	50	6	12	24
Mortar	20	4	8	16
ITZ	16	3	6	12

**Fig. 14.** Homogeneous distribution of three-phase material properties of concrete.**Fig. 15.** Elastic modulus distributions of three-phase materials with different homogeneous degrees.

as a homogeneous medium. However, there are many random micro-pores and defects in mortar and aggregate, which cannot be regarded as an absolutely homogeneous medium. In this section, the homogeneous distribution, random distribution, and spatial correlation distribution of the material properties of each phase at the mesoscale level are considered, respectively. The Weibull statistical distribution function is used to describe the random distribution of material properties, and the spatial correlation function is introduced to consider the correlation and continuity of materials. The proposed model named Concrete Mesoscale Concretization Model (Double CM) can effectively characterize the transition and transformation of mechanical properties from the surface of aggregate to the mortar interior.

**Fig. 16.** Natural rock profile [29] (gray value indicates material property value).

#### 4.1. Homogeneous distribution of three-phase material properties

In most literature, concrete is regarded as a three-phase composite material composed of aggregate, mortar, and ITZ, and the three-phase material properties are homogeneously distributed. That is, each phase material has the same performance at any position. Since the nature of ITZ has not been thoroughly studied at present, this paper assumes that the mechanical properties of ITZ, such as the elastic modulus and strength, are 0.8 times that of mortar. The elastic moduli in Table 4 are assigned to the materials of each phase to obtain the distribution of the internal elastic modulus of concrete, as shown in Fig. 14. The sample size is 100 mm × 100 mm, the mesh size is 0.5 mm, the aggregate content is 40%, and the aggregate particle size is 5–25 mm. In Fig. 14, the darker the color indicates, the greater the elasticity modulus, and this setting is also applied to subsequent figures. It can be observed that the aggregate phase is the strongest material, the ITZ phase is the weakest part in the concrete, and the mortar phase is somewhere in between.

#### 4.2. Random distribution of three-phase material properties

Various defects in the concrete lead to differences in mechanical and physical properties such as strength and elastic modulus in the space. To describe the heterogeneity more reasonably, it is assumed that the mechanical properties of each phase material conform to the Weibull distribution. The density function of the Weibull distribution is shown in Eq. (20).

$$f(u) = \frac{m}{\beta} \left( \frac{u - u_0}{\beta} \right)^{m-1} \exp \left[ - \left( \frac{u - u_0}{\beta} \right)^m \right] \quad (20)$$

where  $u$  is the variable (such as elastic modulus, strength, etc.) that satisfies the Weibull distribution;  $u_0$  is the lower limit of the variable, and  $u_0 = 0.7E(u)$  is used in this paper;  $\beta$  is the scale parameter;  $m$  is the homogeneous degree, and a larger homogeneous degree leads to a more homogeneous distribution of materials.

To compare the influence of the homogeneous degree on the distribution of material properties, three groups of mesoscale models are generated by using the elastic modulus and homogeneous degree in Table 4, as shown in Fig. 15. The elastic modulus distribution of the concrete sample with the lowest homogeneous degree m-1 is the most dispersed. In contrast, the concrete sample with the highest homogeneous degree m-3 has the most homogeneous elastic modulus distribution.

#### 4.3. Spatial correlation distribution of three-phase material properties

There are randomly distributed pores and defects in the mortar, ITZ,

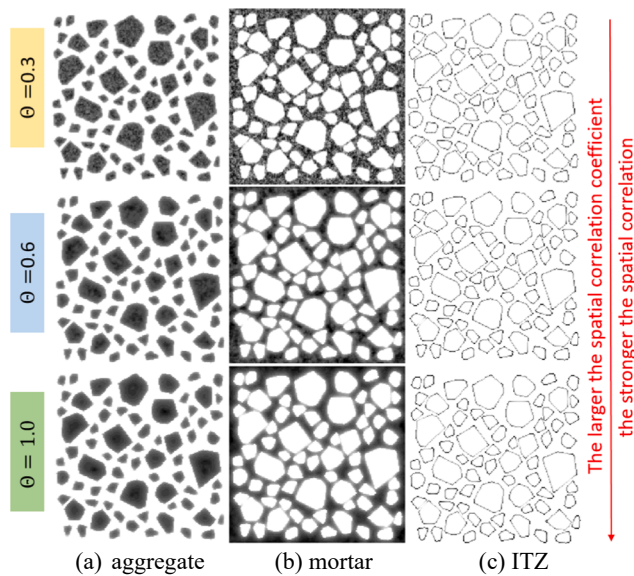


**Fig. 17.** Elastic modulus distributions of three-phase materials with different spatial correlation coefficients.

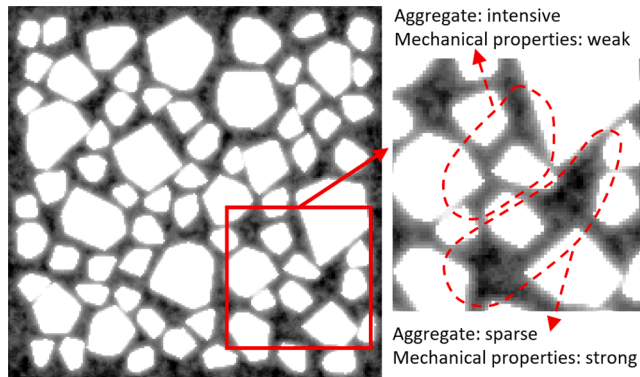


**Fig. 18.** Details of the material properties distribution of the mortar with the spatial correlation coefficient  $\Theta = 0.6$ .

and aggregate of the concrete result in the spatial variation of material properties rather than homogeneity. However, the material properties are not entirely randomly distributed and disorderly but show a specific correlation in the local scope of space, as shown in the natural rock profile [29] in Fig. 16.

To describe the inherent spatial correlation of random field material

properties, Markov spatial correlation function is used in this section. For a specific phase material with total elements of  $n$ , the material property  $f_i$  of element  $i$  is calculated by Eq. (21) and Eq. (22).

$$f_i = \sum_{k=1}^n f_k \rho_{i,k} \quad (21)$$

$$\rho_{i,k} = e^{-\frac{d_{i,k}}{\Theta}} \quad (22)$$

where  $f_i$  and  $f_k$  are the material properties of elements  $i$  and  $k$  respectively;  $\rho_{i,k}$  is the spatial correlation function;  $d_{i,k}$  is the distance between the centroid of element  $i$  and element  $k$ ;  $\Theta$  is the spatial correlation coefficient used to describe the degree of correlation between two points in the space. The larger  $\Theta$  indicates that the stronger the spatial correlation. The transition of the random field becomes smoother with the increase of  $\Theta$ ; on the contrary, the transition becomes more intense.

The material properties updated by the spatial correlation function no longer obey the Weibull distribution, so it needs to be modified. Sort the material properties from small to large, and map them to the Weibull distribution form according to the size order of the material properties to ensure that the material properties conform to the Weibull statistical distribution and satisfy the spatial correlation.

In addition, two aspects need to be noted. (1) The ITZ is actually a part of the mortar matrix with high porosity. In the vicinity of the mortar with good mechanical properties, the mechanical properties of the ITZ are also good. In the vicinity of the mortar with poor mechanical properties, the mechanical properties of the ITZ are often poor. Therefore, the spatial correlation between the mortar and ITZ cannot be considered separately. (2) Since there is no element outside the edge of the concrete sample, the elements at the edge of the concrete calculated by the spatial correlation function are usually the weakest, inconsistent with reality. Therefore, it is necessary to assume a “virtual mortar layer” around the edge of the concrete. The material properties of the ITZ, mortar, and “virtual mortar layer” are first discretized according to the Weibull distribution of the mortar material. Then the material properties considering the spatial correlation are calculated, and finally, the material properties of the ITZ and mortar elements are mapped to their respective Weibull distribution forms, respectively. The material properties of the aggregate elements considering spatial correlation are calculated separately.

The concrete sample with the homogeneous degree  $m-1$  in Fig. 15 is modified according to the spatial correlation function to obtain the elastic modulus distribution of concrete with different spatial correlation coefficients  $\Theta$ , as shown in Fig. 17. A small spatial correlation coefficient ( $\Theta = 0.3$ ) has little effect on the random field. Excessive spatial correlation coefficient ( $\Theta = 1.0$ ) leads to too strong spatial correlation and makes the material properties appear the “circle-shaped” phenomenon. Compared with the natural material profile in Fig. 16, the moderate spatial correlation coefficient ( $\Theta = 0.6$ ) is the most consistent with

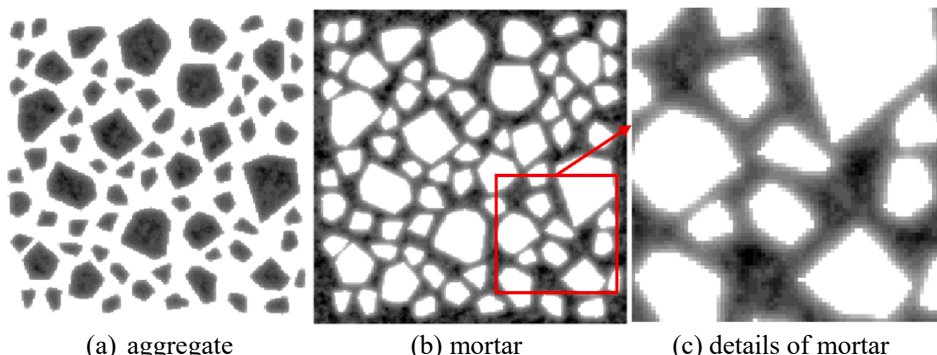


**Fig. 19.** Elastic modulus distributions of two-phase materials with the spatial correlation coefficient  $\Theta = 0.6$ .

the actual material property distributions.

The specific details of the material property distribution of the mortar phase with the spatial correlation coefficient  $\Theta = 0.6$  are shown in Fig. 18. In areas where aggregates are dense, the elastic modulus of mortar is low, and the mechanical properties are poor. In areas where aggregates are sparse, the elastic modulus of mortar is high, and the mechanical properties are strong. In actual concrete, the bleeding phenomenon is obvious in the area with dense aggregate, which leads to the high porosity of the mortar and the decrease of the corresponding mechanical properties. The randomness, continuity, and spatial correlation of materials in all phases are consistent with actual cognition, indicating that the material properties assignment in this section is credible.

#### 4.4. Spatial correlation distribution of two-phase material properties

Before this section, concrete is considered a three-phase composite material composed of aggregate, mortar, and ITZ. The ITZ is actually a part of the mortar matrix with high porosity. Since the mechanical properties of the ITZ are similar to that of mortar, the ITZ can be considered as the “weak” mortar, and concrete can be regarded as a two-phase composite material composed only of aggregate and mortar. The Weibull statistical distribution function is used to describe the random distribution of material properties, and the spatial correlation function is used to consider the correlation and continuity of materials.

The mortar and “virtual mortar layer” material properties are first discretized according to the Weibull distribution form of the mortar material, and then the material properties of the mortar considering the spatial correlation are calculated. The material properties of the aggregate elements considering spatial correlation are calculated separately. The elastic modulus and homogeneous degree  $m-1$  in Table 4 are used for calculating the material property distributions of the mortar and aggregate under the condition that the spatial correlation coefficient  $\Theta = 0.6$ , as shown in Fig. 19. Due to the existence of wall effect and bleeding, the mortar around the surface of the aggregate has a high porosity and shows poor mechanical properties. Even without the use of ITZ elements, the proposed method in this section can effectively characterize the transition and transformation of mechanical properties from the surface of aggregate to the interior of mortar. Moreover, the elastic modulus of mortar is low and the mechanical properties are poor in the area with dense aggregates. In the area where aggregates are sparse, the elastic modulus of mortar is high and the mechanical properties are strong.

### 5. Numerical simulations of uniaxial tension

#### 5.1. Constitutive model and boundary conditions

##### 5.1.1. Introduction to the CDP model

For ordinary concrete, the strength of aggregate is much greater than that of mortar and ITZ. Therefore, it is assumed that the aggregate remains elastic during the entire loading process, while the mortar and ITZ show damage and elastoplastic behavior before failure [30]. In this paper, the CDP (Concrete Damage Plastic) model in the ABAQUS material library is used as the constitutive model to describe the damage and stiffness degradation of the mortar and ITZ [31]. There are already many descriptions of the CDP model, so it will not be introduced here. For specific descriptions, please refer to the literature [32–34] and ABAQUS Analysis User’s Guide.

Before reaching the ultimate tensile strength and compressive yield stress, the stress-strain relationship of the mortar and ITZ is assumed linear elastic for simplicity. For uniaxial compression, Eq. (23) is adopted to describe the post-peak softening behavior [35].

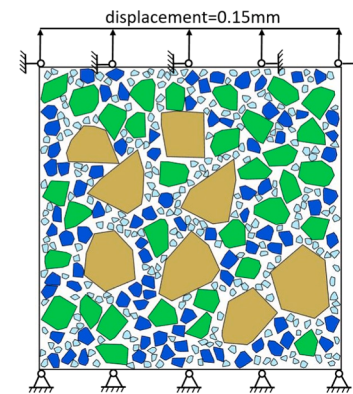


Fig. 20. Boundary conditions for numerical concrete model.

Table 5

Material properties of each phase of concrete in numerical simulation.

Material properties	Aggregate	Mortar	ITZ
Density $\rho(\text{kg}/\text{m}^3)$	2600	2200	2200
Elasticity modulus $E(\text{GPa})^*$	50	20	16
Poisson ratio $\mu$	0.16	0.2	0.2
Homogeneous degree $m$	6	4	3
Spatial correlation coefficient $\Theta$	0.6	0.6	0.6
Compressive strength $\sigma_{cu}(\text{MPa})^*$	–	40	32
Tensile strength $\sigma_{tu}(\text{MPa})^*$	–	3.5	2.8
Fracture energy $G_F(\text{N/m})^*$	–	100	80

$$\frac{\sigma_c}{\sigma_{cu}} = \begin{cases} \alpha_a \frac{\varepsilon_c}{\varepsilon_{cu}} + (3 - 2\alpha_a) \left( \frac{\varepsilon_c}{\varepsilon_{cu}} \right)^2 + (\alpha_a - 2) \left( \frac{\varepsilon_c}{\varepsilon_{cu}} \right)^3, & \frac{\sigma_c}{\sigma_{cu}} \geq 0.4 \text{ and } \frac{\varepsilon_c}{\varepsilon_{cu}} \leq 1 \\ \frac{\varepsilon_c}{\varepsilon_{cu}}, & \frac{\varepsilon_c}{\varepsilon_{cu}} > 1 \\ \alpha_d \left( \frac{\varepsilon_c}{\varepsilon_{cu}} - 1 \right)^2 + \frac{\varepsilon_c}{\varepsilon_{cu}}, & \frac{\varepsilon_c}{\varepsilon_{cu}} > 1 \end{cases} \quad (23)$$

where  $\varepsilon_c$  and  $\sigma_c$  are the compressive strain and compressive stress respectively,  $\varepsilon_{cu}$  is the peak strain corresponding to the ultimate compressive strength of  $\sigma_{cu}$ , and  $\alpha_a$  and  $\alpha_d$  are the coefficients calculated by  $\alpha_a = 2.4 - 0.0125\sigma_{cu}$  and  $\alpha_d = 0.157\sigma_{cu}^{0.785} - 0.905$ .

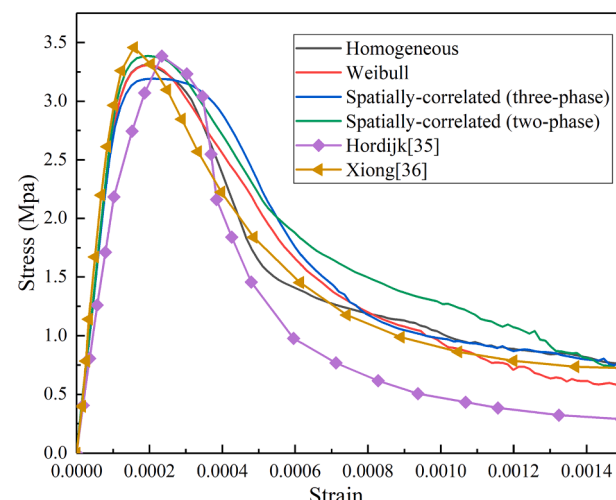


Fig. 21. Comparison of uniaxial tensile stress-strain curves of concrete with different material properties distribution types and results in [36–37].

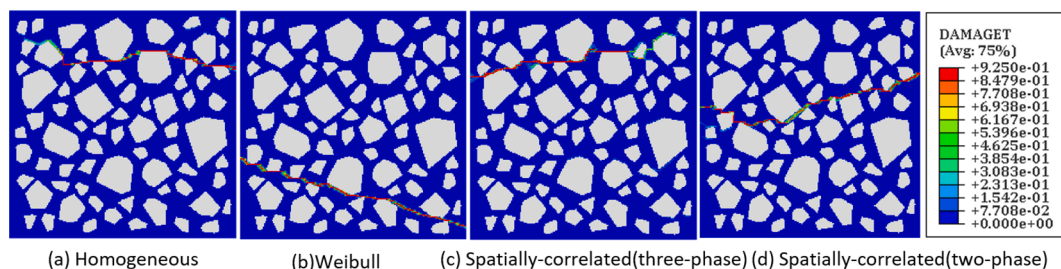


Fig. 22. Tensile failure modes of concrete with different material properties distributions.

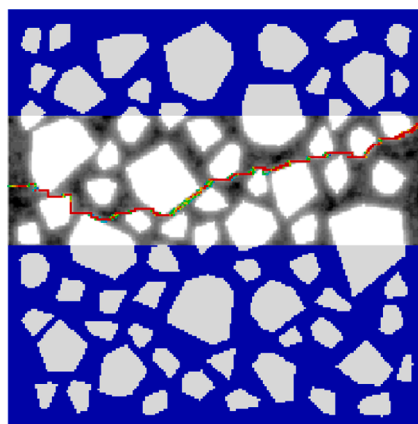


Fig. 23. Crack patterns of concrete with material properties distribution of spatial-correlated (two-phase) subjected to uniaxial tensile loading.

To avoid unreasonable mesh sensitivity in the results, the tensile softening behavior is defined by the criterion based on linear fracture energy instead of the tensile stress-strain curve [34]. The keywords \*CONCRETE TENSION STEFFEINING, TYPE = DISPLACEMENT is used to define the tensile softening behavior based on the linear fracture energy criterion [32]. The ABAQUS/Explicit module is used for finite element analysis, and the software automatically ignores the viscosity parameter. In addition, four parameters need to be determined for the CDP model, that is, dilation angle: 30°, flow potential eccentricity: 0.1, the ratio of initial equibiaxial compressive yield stress to initial uniaxial compressive yield stress: 1.16, and the ratio of the second stress invariant on the tensile meridian: 0.667.

### 5.1.2. Boundary conditions setting

In order to obtain the load and displacement response of concrete samples during the tensile process, the displacement control method is adopted for the tensile loading protocol. The nodes of finite elements at the bottom of the calculation model are fixed. The nodes at the top of the model are applied with a uniformly increasing displacement with time perpendicular to the loading surface, and the horizontal degrees of freedom are constrained, as shown in Fig. 20. On the one hand, to ensure quasi-static loading, the loading time should be long enough to avoid any dynamic response. On the other hand, the computational cost increases with the increase of loading time. In the subsequent simulations, the loading displacement is set as 0.15 mm, and the loading time is 0.1 s. According to the simulation results, the ratio of total kinetic energy to total internal energy is always less than 5% to ensure a sufficiently small dynamic response [8,16].

### 5.2. Model verification

The material properties of each phase of concrete have an essential influence on the numerical simulation results of uniaxial tension. The material properties of each phase used in the simulations in this paper

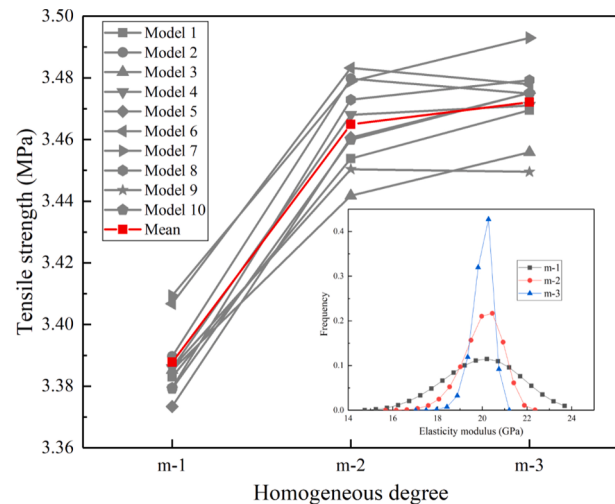


Fig. 24. Effect of homogeneous degree on tensile strength of concrete.

are shown in Table 5. It should be noted that the material properties with the “\*\*” superscript in Table 5 represent the mean when the material properties are inhomogeneously distributed.

For the convenience of expression, the following codes are used to represent different material properties assignment methods. (1) Homogeneous represents the homogeneous distribution of three-phase material properties. (2) Weibull represents the random distribution satisfying Weibull's statistical function of three-phase material properties. (3) Spatially-correlated (three-phase) represents the spatial correlation distribution of three-phase material properties. (4) Spatially-correlated (two-phase) represents the spatial correlation distribution of two-phase material properties.

Fig. 21 shows the comparison between uniaxial tensile stress-strain curves of concrete with different material properties assignment types and experimental results in [36] and simulation results in [37]. It can be seen from Fig. 21 that the stress-strain curves obtained by uniaxial tensile simulations of concrete with four different material properties assignment types in this paper are in good agreement with the test results in [36] and the numerical simulation results in [37], which verifies the applicability of the four material properties assignment methods proposed in this paper. Due to the differences in the mechanical properties of each phase material, aggregate content, aggregate distribution in the simulations in this paper and the literature [36–37], it is meaningless to compare these curves accurately and quantitatively.

In addition, different distribution types of material properties lead to the different weak parts of concrete under tensile load, resulting in different crack patterns of concrete, as shown in Fig. 22. Fig. 23 shows the crack patterns of concrete with material properties distribution of Spatial-correlated (two-phase) subjected to uniaxial tensile loading. The mortar around the aggregate is the weak part of the concrete. Under uniaxial tensile load, cracks always appear here first and extend into the mortar interior. Concrete is regarded as a two-phase composite material

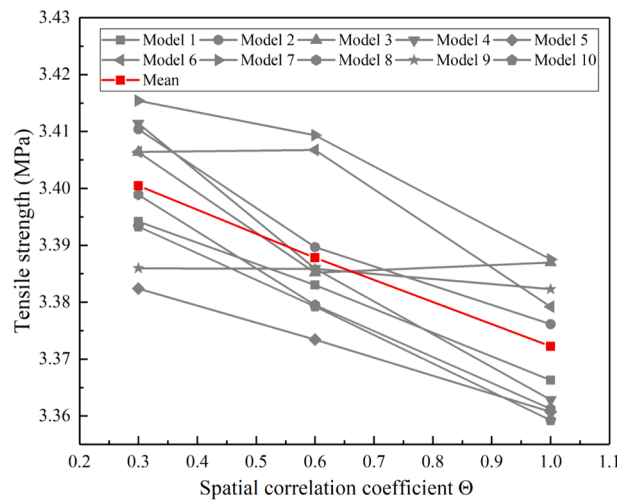


Fig. 25. Effect of spatial correlation coefficient on tensile strength of concrete.

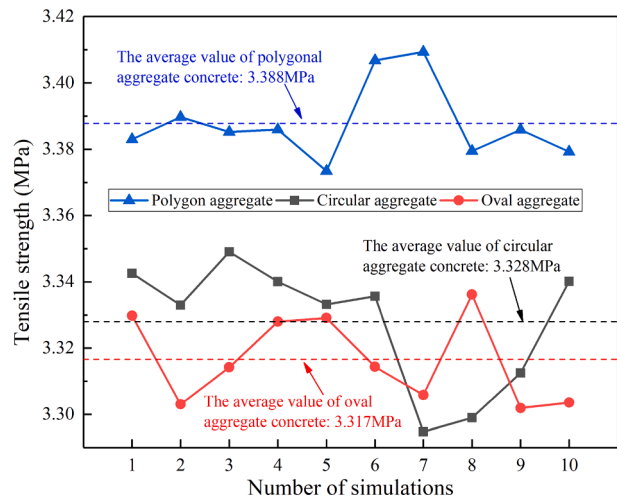


Fig. 26. Tensile strength of concrete with aggregates of different shapes.

composed only of aggregate and mortar by the material attribute assignment method of spatial-correlated (two-phase). The randomness, continuity, and spatial correlation are considered in the distribution of material properties. The crack patterns are consistent with actual cognition, indicating that this material properties assignment is more realistic and effective. In the following numerical simulations, material properties are assigned by the Spatial-correlated (two-phase) method.

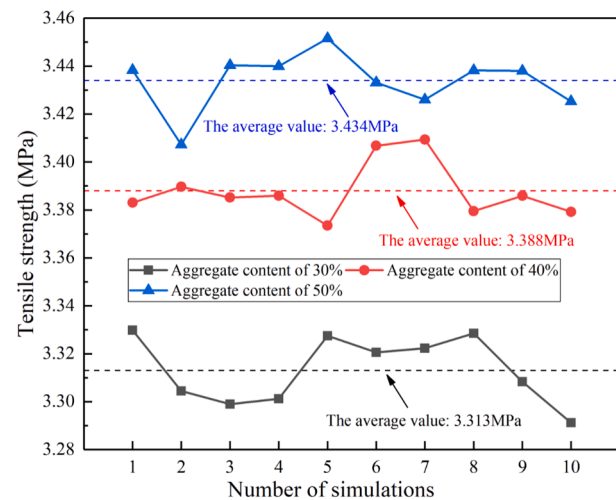


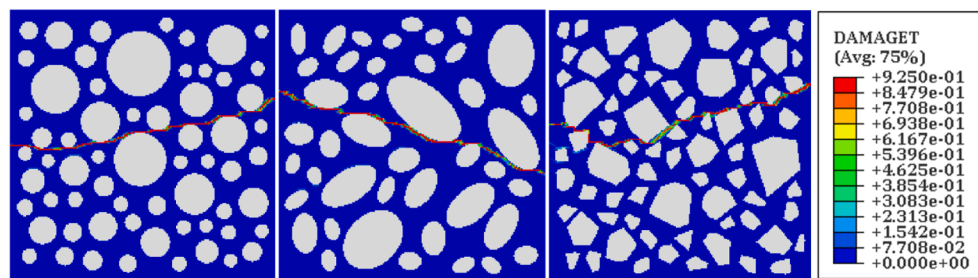
Fig. 28. Tensile strength of concrete with different aggregate contents.

### 5.3. Effects of homogeneous degree and spatial correlation coefficient on tensile strength

#### 5.3.1. Effect of homogeneous degree on tensile strength

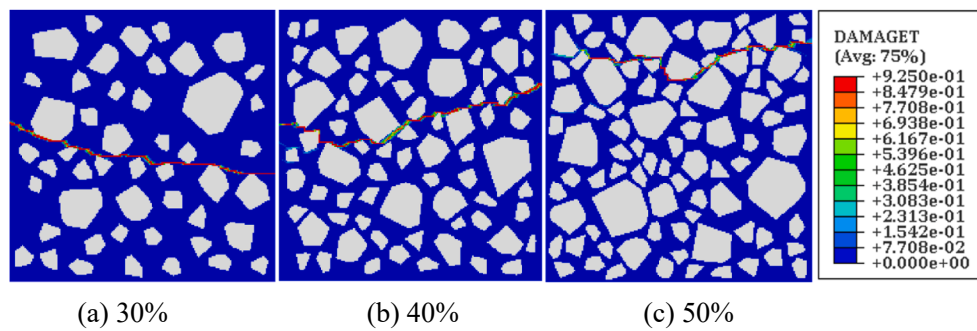
The homogeneous degree reflects the uniformity of distribution of material properties. A larger homogeneous degree leads to a more homogeneous distribution of materials. In this section, ten mesoscale models with different aggregate distributions are simulated under uniaxial tension. The aggregate information and concrete sizes are the same as those in Section 4, and the spatial correlation coefficient is 0.6. In addition, m-1, m-2, and m-3 ( $m_3 > m_2 > m_1$ ) in Table 4 are used as homogeneous degrees of aggregate and mortar, and the parameters in Table 5 are used for other material properties.

Fig. 24 shows the tensile strength of concrete mesoscale models with different homogeneous degrees. With the increase of homogeneous degree, the tensile strength of concrete tends to increase. When the homogeneous degree increases from m-1 to m-2, the tensile strength increases significantly, but when the homogeneous degree increases from m-2 to m-3, the tensile strength increases little or even remains the same. According to Eq. (20), the homogeneous degree controls the degree of deviation of the material properties from the mean value. The greater the homogeneous degree, the smaller the deviation of the material properties from the mean value. Under uniaxial tensile load, cracks always initiate from the weak parts around the aggregate and penetrate the mortar. The improvement of homogeneous degree leads to the material properties of these weak parts to increase towards the mean value, thus improving the tensile strength of concrete. Compared with m-2, the excessively high homogeneous degree m-3 does not significantly reduce the weak elements, so the improvement of the tensile strength of concrete is not apparent.



(a) circular aggregate    (b) oval aggregate    (c) polygonal aggregate

Fig. 27. Tensile failure modes of concrete with aggregate of different shapes.



**Fig. 29.** Tensile failure modes of concrete with different aggregate contents.

### 5.3.2. Effect of spatial correlation coefficient on tensile strength

The spatial correlation coefficient represents the degree of spatial correlation of material properties. For the ten models with homogeneous degree  $m=1$  in Section 5.3.1, the tensile strength of concrete with different spatial correlation coefficients is simulated. It can be seen from Fig. 25 that the tensile strength of concrete tends to decrease with the increase of the spatial correlation coefficient. The increase of spatial correlation coefficient represents the enhancement of the degree of spatial correlation, which leads to the concentration of weak parts in the mesoscale model and the decrease of tensile strength of concrete.

## 5.4. Effect of aggregate on simulation results

### 5.4.1. Effect of aggregate shape on tensile strength

The aggregates used to prepare concrete are usually pebbles and crushed stones. In the 2-D case, circular and oval aggregates are usually used to represent pebbles, and polygonal aggregates are used to represent crushed stones. Ten mesoscale models with different aggregate distributions are simulated under uniaxial tension for concretes with different shapes of aggregates. The aggregate information and concrete sizes are the same as those in Section 4. The homogeneous degree is  $m=1$  and the spatial correlation coefficient  $\Theta = 0.6$ . It can be seen from Fig. 26 that the concrete with the polygonal aggregates has the highest tensile strength (the average value is 3.388 MPa). In contrast, the concrete with circular aggregates and oval aggregates have similar tensile strength (the average values are 3.328 MPa and 3.317 MPa, respectively). Compared with the circular and oval aggregates, polygonal aggregates usually have distinct edges and corners. For the same aggregate content, polygonal aggregates tend to have larger surface areas. Under uniaxial tensile load, the crack propagation path of concrete with polygonal aggregate is more tortuous, which increases the difficulty of crack propagation and leads to the high tensile strength of concrete, as shown in Fig. 27.

### 5.4.2. Effect of aggregate content on tensile strength

Aggregate has two effects on the tensile performance of concrete: on the one hand, aggregate can hinder the path of crack propagation and improve the tensile strength of concrete; on the other hand, the weak parts around the aggregate have worse performance than mortar, which reduces the tensile strength of concrete. To analyze the effect of aggregate content on the tensile performance of concrete, uniaxial tensile numerical simulations are carried out for polygonal aggregate concrete with 30%, 40%, and 50% aggregate content, respectively. The model information and material parameters are the same as those in Section 5.4.1, and the simulation results are shown in Fig. 28 and Fig. 29.

It can be seen from Fig. 28 and Fig. 29 that the tensile strength of concrete increases with the increase of aggregate content. When the aggregate content is 30%, 40%, and 50%, the average tensile strength of the ten models is 3.313 MPa, 3.388 MPa, and 3.434 MPa, respectively. Therefore, the increase of aggregate content has a more substantial hindering effect on crack propagation than the negative effect of weak

parts around the aggregate. On the premise of ensuring the workability of concrete, it is recommended to add more aggregates to improve the tensile strength of concrete.

## 6. Conclusions

- (1) A complete procedure named “mesh – placement – identification – assignment” (MPIA) is proposed to establish the mesoscale model and assign material properties to each phase.
- (2) Four different methods for assigning material properties are introduced respectively, which are Homogeneous, Weibull, Spatially-correlated (three-phase), Spatially-correlated (two-phase).
- (3) Considering the ITZs as a part of mortar, the concrete is regarded as a two-phase composite material composed of aggregate and mortar. The randomness, continuity, and spatial correlation of materials are considered using the Spatially-correlated (two-phase) method. The proposed model named Concrete Mesoscale Concretization Model (Double CM) can effectively characterize the transition and transformation of mechanical properties from the surface of aggregate to the mortar interior. The crack patterns are consistent with actual cognition, indicating that this material properties assignment is more realistic and practical.
- (4) The effects of homogeneous degree and spatial correlation coefficient on the uniaxial tensile simulation results of concrete are studied. The effects of aggregate shape and aggregate content on the tensile strength of concrete are discussed. The results show that the tensile strength of concrete can be improved by increasing the homogeneous degree, increasing the aggregate content, and using crushed stone aggregate. The increase of the spatial correlation coefficient will result in the concentrated distribution of the weak parts in concrete and decrease the tensile strength of concrete.

In this paper, uniaxial tensile numerical simulations of concrete are carried out only in the 2-D case. Still, the mesoscale model in this paper is also applicable to uniaxial compression simulation and 3-D numerical simulation. The randomness, continuity, and spatial correlation of materials in concrete can describe the mechanical properties and characterize the compactness of materials. Therefore, they can also be associated with other physical properties such as permeability or diffusion, which will lead to more meaningful topics.

### CRediT authorship contribution statement

**Zhishan Zheng:** Conceptualization, Methodology, Software, Validation, Formal analysis, Investigation, Resources, Data curation, Writing – original draft, Writing – review & editing, Visualization, Supervision, Project administration. **Xiaosheng Wei:** Validation, Resources, Data curation, Writing – review & editing, Funding acquisition. **Cong Tian:** Validation, Resources, Data curation, Writing – review &

editing.

## Declaration of Competing Interest

The authors declare that they have no known competing financial interests or personal relationships that could have appeared to influence the work reported in this paper.

## Acknowledgments

Support from the National Natural Science Foundation of China (grant number 51778257) is gratefully acknowledged.

## References

- [1] Z. Wu, J. Zhang, H. Yu, et al., 3D mesoscopic investigation of the specimen aspect-ratio effect on coral aggregate concrete[J], Composites Part B Engineering (2020) 108025, <https://doi.org/10.1016/j.compositesb.2020.108025>.
- [2] D. Ma, Z. Liang, Y. Liu, Z. Jiang, Z. Liu, L. Zhou, L. Tang, Mesoscale modeling of epoxy polymer concrete under tension or bending[J], Composite Structures 256 (2021) 113079, <https://doi.org/10.1016/j.compstruct.2020.113079>.
- [3] X.F. Wang, Z.J. Yang, J.R. Yates, A.P. Jivkov, C.h. Zhang, Monte Carlo simulations of mesoscale fracture modelling of concrete with random aggregates and pores[J], Construction and Building Materials 75 (2015) 35–45, <https://doi.org/10.1016/j.conbuildmat.2014.09.069>.
- [4] Z. Zhang, X. Song, Y. Liu, D.i. Wu, C. Song, Three-dimensional mesoscale modelling of concrete composites by using random walking algorithm[J], Composites science & Technology 149 (2017) 235–245, <https://doi.org/10.1016/j.compscitech.2017.06.015>.
- [5] X. Li, X. Chen, A.P. Jivkov, J. Zhang, 3D mesoscale modeling and fracture property study of rubberized self-compacting concrete based on uniaxial tension test[J], Theoretical and Applied Fracture Mechanics 104 (2019) 102363, <https://doi.org/10.1016/j.tafmec.2019.102363>.
- [6] X. Du, L. Jin, Meso-scale numerical investigation on cracking of cover concrete induced by corrosion of reinforcing steel[J], Engineering Failure Analysis 39 (2014) 21–33, <https://doi.org/10.1016/j.engfailanal.2014.01.011>.
- [7] R. Zhou, Z. Song, Y. Lu, 3D mesoscale finite element modelling of concrete[J], Computers & Structures 192 (2017) 96–113, <https://doi.org/10.1016/j.compstruc.2017.07.009>.
- [8] J. Xiao, W. Li, D.J. Corr, S.P. Shah, Effects of interfacial transition zones on the stress-strain behavior of modeled recycled aggregate concrete[J], Cement & Concrete Research 52 (2013) 82–99, <https://doi.org/10.1016/j.cemconres.2013.05.004>.
- [9] P.S.M. Thilakarathna, K.S. Kristombu Baduge, P. Mendis, E.R.K. Chandrathilaka, V. Vimonsatit, H. Lee, Understanding fracture mechanism and behaviour of ultra-high strength concrete using mesoscale modelling[J], Engineering Fracture Mechanics 234 (2020) 107080, <https://doi.org/10.1016/j.engfracmech.2020.107080>.
- [10] Y. Huang, Z. Yang, W. Ren, G. Liu, C. Zhang, 3D meso-scale fracture modelling and validation of concrete based on in-situ X-ray Computed Tomography images using damage plasticity model[J], International Journal of Solids and Structures 67–68 (2015) 340–352, <https://doi.org/10.1016/j.ijsolstr.2015.05.002>.
- [11] P.S.M. Thilakarathna, K.S. Kristombu Baduge, P. Mendis, V. Vimonsatit, H. Lee, Mesoscale Modelling of Concrete – A Review of Geometry Generation, Placing Algorithms, Constitutive Relations and Applications[J], Engineering Fracture Mechanics 231 (2020) 106974, <https://doi.org/10.1016/j.engfracmech.2020.106974>.
- [12] Y. Sun, X. Wei, H. Gong, C. Du, W. Wang, J. Chen, A two-dimensional random aggregate structure generation method: Determining effective thermo-mechanical properties of asphalt concrete[J], Mechanics of Materials 148 (2020) 103510, <https://doi.org/10.1016/j.mechmat.2020.103510>.
- [13] Q.-X. Meng, D. Lv, Y. Liu, Mesoscale computational modeling of concrete-like particle-reinforced composites with non-convex aggregates[J], Computers & Structures 240 (2020) 106349, <https://doi.org/10.1016/j.compstruc.2020.106349>.
- [14] H. Ouyang, X. Chen, 3D meso-scale modeling of concrete with a local background grid method[J], Construction and Building Materials 257 (2) (2020), 119382, <https://doi.org/10.1016/j.conbuildmat.2020.119382>.
- [15] Y. Zhang, Q. Chen, Z. Wang, J. Zhang, Z. Wang, Z. Li, 3D mesoscale fracture analysis of concrete under complex loading[J], Engineering Fracture Mechanics 220 (2019) 106646, <https://doi.org/10.1016/j.engfracmech.2019.106646>.
- [16] S. Naderi, W. Tu, M. Zhang, Meso-scale modelling of compressive fracture in concrete with irregularly shaped aggregates[J], Cement and Concrete Research 140 (2021) 106317, <https://doi.org/10.1016/j.cemconres.2020.106317>.
- [17] M. Khormani, V.R. Kalat Jaari, I. Aghayan, S.H. Ghaderi, A. Ahmadyfard, Compressive strength determination of concrete specimens using X-ray computed tomography and finite element method[J], Construction and Building Materials 256 (2020) 119427, <https://doi.org/10.1016/j.conbuildmat.2020.119427>.
- [18] X. Ruan, Y. Li, Z. Jin, Z. Pan, Z. Yin, Modeling method of concrete material at mesoscale with refined aggregate shapes based on image recognition[J], Construction and Building Materials 204 (2019) 562–575, <https://doi.org/10.1016/j.conbuildmat.2019.01.157>.
- [19] X. Qin, C. Gu, C. Shao, X. Fu, L. Vallejo, Y. Chen, Numerical analysis of fracturing behavior in fully-graded concrete with oversized aggregates from mesoscopic perspective[J], Construction and Building Materials 253 (2020) 119184, <https://doi.org/10.1016/j.conbuildmat.2020.119184>.
- [20] W.C. Zhu, J.G. Teng, C.A. Tang, Mesomechanical Model for Concrete. Part I: Model Development[J], Magazine of Concrete Research 56 (6) (2004) 313–330, <https://doi.org/10.1680/macr.2004.56.6.313>.
- [21] J.G. Teng, W.C. Zhu, C.A. Tang, Mesomechanical model for concrete. Part II: applications[J], Magazine of Concrete Research 56(6):p.331-345 (2004), <https://doi.org/10.1680/macr.2004.56.6.331>.
- [22] H. Jin, Y. Zhou, B. Wang, S. Zhou, Mesoscopic Finite Element Modeling of Concrete Considering Geometric Boundaries of Actual Aggregates[J], Advances in Materials Science and Engineering 2018 (2018) 1–10, <https://doi.org/10.1155/2018/7816502>.
- [23] Zheng Z, Wei X. Mesoscopic models and numerical simulations of the temperature field and hydration degree in early-age concrete [J]. Construction and Building Materials, 266. <https://doi.org/10.1016/j.conbuildmat.2020.121001>.
- [24] Y. Yu, Y.u. Zheng, Y. Guo, S. Hu, K. Hua, Mesoscale finite element modeling of recycled aggregate concrete under axial tension[J], Construction and Building Materials 266 (2021) 121002, <https://doi.org/10.1016/j.conbuildmat.2020.121002>.
- [25] Z. Zhu, W. Xu, H. Chen, The fraction of overlapping interphase around 2D and 3D polydisperse non-spherical particles: Theoretical and numerical models[J], Computer Methods in Applied Mechanics and Engineering 345 (2019) 728–747, <https://doi.org/10.1016/j.cma.2018.11.022>.
- [26] Z. Qian, E. Schlangen, G. Ye, Modeling Framework for Fracture in Multiscale Cement-Based Material Structures[J], Materials 10 (6) (2017) 587, <https://doi.org/10.3390/ma10060587>.
- [27] H. Kai, A. Agathos, The point in polygon problem for arbitrary polygons[J], Computational Geometry 20 (3) (2001) 131–144, [https://doi.org/10.1016/S0925-7721\(01\)00012-8](https://doi.org/10.1016/S0925-7721(01)00012-8).
- [28] X.W. Tang, C.H. Zhang, J.J. Shi, A multiphase mesostructure mechanics approach to the study of the fracture-damage behavior of concrete[J], Science in China 51 (2 Supplement) (2008) 8–24, <https://doi.org/10.1016/B978-0-12-408083-6.00024-6>.
- [29] N. Cho, C.D. Martin, D.C. Sego, A clumped particle model for rock[J], International Journal of Rock Mechanics & Mining Sciences 44 (7) (2007) 997–1010, <https://doi.org/10.1016/j.ijrmms.2007.02.002>.
- [30] Y. Zhou, H. Jin, B. Wang, Modeling and mechanical influence of meso-scale concrete considering actual aggregate shapes[J], Construction and Building Materials 228 (2019) 116785, <https://doi.org/10.1016/j.conbuildmat.2019.116785>.
- [31] H. Chen, B. Xu, J. Wang, T. Zhou, X. Nie, Y.L. Mo, Parametric analysis on compressive strain rate effect of concrete using mesoscale modeling approach[J], Construction and Building Materials 246 (2020) 118375, <https://doi.org/10.1016/j.conbuildmat.2020.118375>.
- [32] H. Chen, B. Xu, Y.L. Mo, T. Zhou, Behavior of meso-scale heterogeneous concrete under uniaxial tensile and compressive loadings[J], Construction and Building Materials 178 (2018) 418–431, <https://doi.org/10.1016/j.conbuildmat.2018.05.052>.
- [33] L. Jin, C. Xu, Y. Han, X. Du, Effect of End Friction on the Dynamic Compressive Mechanical Behavior of Concrete under Medium and Low Strain Rates[J], Shock and Vibration 2016 (2016) 1–20, <https://doi.org/10.1155/2016/6309073>.
- [34] X. Du, L. Jin, G. Ma, Numerical simulation of dynamic tensile-failure of concrete at meso-scale[J], International Journal of Impact Engineering 66 (2014) 5–17, <https://doi.org/10.1016/j.ijimpeng.2013.12.005>.
- [35] Z. Guo, X. Zhang, D. Zhang, R. Wang, Experimental investigation of the complete stress–strain curve of concrete, J. Build. Struct. 3 (1982) 1–12.
- [36] D.A. Hordijk, Tensile and tensile fatigue behaviour of concrete; experiments, modelling and analyses[J], Heron 37 (1) (1992) 1–79. <http://worldcat.org/issn/00467316>.
- [37] Q. Xiong, X. Wang, A.P. Jivkov, A 3D multi-phase meso-scale model for modelling coupling of damage and transport properties in concrete[J], Cement and Concrete Composites 109 (2020) 103545, <https://doi.org/10.1016/j.cemconcomp.2020.103545>.